Antibacterial and Cell-Viability of Hydroxyapatite Derived from Waste Marine Shell for Biomedical Applications

G. Suresh[1,*,], K. Dhanaraj[2,], R.N. Viswanath[1,], B. Dhanalakshmi[1,] and A. Sindhya[3,]

[1]Department of Physics, Centre for Nanotechnology Research, Aarupadai Veedu Institute of Technology, Vinayaka Mission's Research Foundation (D U), Chennai-603104, India
[2]Department of Physics, St. Joseph's College of Engineering, Sholinganallur, Chennai, India
[3]Department of Science and Humanities/Physics, I.F.E.T. College of Engineering (Autonomous), Villupuram-605108, India

*Corresponding author: E-mail: suresh.physics@avit.ac.in

The present study discusses on the functional groups, structural characterization and thermal behaviour of *Crassostrea angulata* shell used for the synthesis of a biocompatible hydroxyapatite material. The hydroxyapatite was synthesized from *C. angulata* shell through precipitation method and characterized using XRD, FTIR, FE-SEM, EDX mapping, HR-TEM and SAED pattern. The formation of hydroxyapatite was confirmed from the high intense X-ray diffraction lines and by the presence of chemical groups such as PO_4^{3-}, OH^- and CO_3^{2-}. The structural changes during the formation of hydroxyapatite from the thermal decomposition of *C. angulata* shell were studied through XRD and TG-DTA. The morphology study by FE-SEM indicates that the synthesized hydroxyapatite materials were in the form of clusters of rod-like particles. The SAED patterns and XRD spectral lines confirmed the crystalline nature of the synthesized hydroxyapatite. The antibacterial activity and cell viability assay of prepared hydroxyapatite were studied to assess its suitability in various biomedical applications. The antibacterial activity of hydroxyapatite was assessed against Gram-negative (*Escherichia coli*) and Gram-positive (*Staphylococcus saprophyticus*) bacterial strains. The cytocompatibility of hydroxyapatite was assessed through an MTT assay using osteoblast cells (MG-63 cell). Thus, the prepared hydroxyapatite shows good antibacterial action and cell viability nature and it can be applied in various biomedical applications.

Keywords: *Crassostrea angulata*, Hydroxyapatite, Antibacterial activity, Cell viability.

INTRODUCTION

Hydroxyapatite [$(Ca_{10}(PO_4)_6(OH)_2)$] is a member of the calcium phosphate family, which fascinates significant consideration due to its remarkable progress from a biomaterial to an advanced functional material in materials science field [1]. Human calcified tissues consist of hydroxyapatite, an inorganic component, which is highly significant [2]. It crystallizes in the most common hexagonal crystal system and belongs to the space group $P6_3/m$ with cell parameters a = b = 9.418 Å and c = 6.884 Å. Its structure includes a range of PO_4^{3-} tetrahedra, which are kept together by Ca^{2+} ions scattered among them. The Ca^{2+} ions are appeared in two distinct locations (aligned columns) (Ca^+ and Ca^{2+}) and the neighbouring OH^- ion in conflicting directions [1]. Because of its structural benefits, biocompatibility, non-inflammatory properties, active surface, easy

modification, inimitable chemical and physical properties, tailorable size and non-toxic, hydroxyapatite has sparked interest in its applications as tissue engineering systems, drug delivery and dental material [3]. Especially, in recent years, research involving biomedical applications using hydroxyapatite are becoming protuberant [4] due to its two critical properties such as enhanced biocompatibility and biodegradability.

Hydroxyapatite is used often for bone implants for regenerating bone tissues. However, the literature reported that the hydroxyapatite products induce implantation failure and bring serious complications after surgical operations due to improper optimization of the hydroxyapatite [5]. Therefore, it is essential to investigate the antibacterial properties and cell viability of hydroxyapatite before using it for implants. The antibacterial activity of a biomaterial is closely linked to the complexes

that selectively eliminate bacteria or inhibit their growth without causing any toxicity [6,7]. For evaluating biological activity, the cytotoxicity is one of the most significant approaches which practices tissue cells *in vitro* to observe the cell growth and it has several advantages such as simple, fast and high sensitivity [8]. The synthesis of hydroxyapatite with good antibacterial and cell viability activity could be an intriguing solution. As reported in the literatures, hydroxyapatite could inhibit good bacterial growth [7,9-11] and cell viability nature [12-18]. Hydroxyapatite in its nano-form has a higher surface area to volume ratio, which makes it effective in preventing bacterial growth and promoting cell viability [18].

Marine shells are mostly self-possessed of inorganic phase $CaCO_3$ (calcite, aragonite, spherulite and amorphous forms) (about 95%) and about 5% organic phase (polysaccharides, glycoproteins, proteins, lipid, chitin, *etc.*) and their complex composition exhibits it valuable for abuse in both inorganic and organic materials [19,20]. However, their disposal environmental pollution is enormous due to the 2700 billion tons of wastes are formed every year. Amongst, only 450-1000 billion waste could be used for many uses. The remaining amount (about 50%) is being deposited as undesirable biowaste. The progressive accumulation of waste disposed shells are possible in marine water, which makes excessive effect on the environment. The management of the shells is a challenging problem [21], moreover, decomposition of shells takes a long period which leads to pose a serious environmental and ecological problems by the way of decrease the land quality, destruct the renewable natural possessions and infect aquatic organisms [19]. Thus, the proper utilization of waste shells which convert into the value-added products including hydroxyapatite without any environmental and health issues is necessary.

Interestingly, the waste shells are composed of calcium carbonate ($CaCO_3$) in aragonite crystalline polymorph at room temperature. The main component of shells calcium carbonate is converted into calcium oxide (CaO) at high-temperature calcination. Its chemical structure, volume, grain size and bond length (morphology and crystallography properties) are meaningfully altered [19]. The CaO derived from marine shell wastes is effectively used to synthesize the hydroxyapatite [22]. Biogenic waste is abundant in nature and has several interesting physico-chemical features, including a large surface area, shape, functions, and structure [23]. Among the various studied shells, the *Crassostrea angulata* (oyster) is a highly abundant and natural biomineralized material which consists of $CaCO_3$ (up to 95%) and Ca, Fe, Cu, Al, *etc* and produces 120,000 tons/year of oyster shells [24].
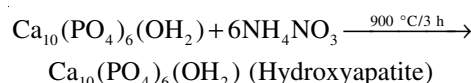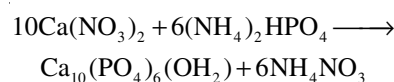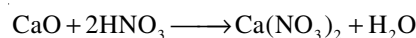
In present study, the functional, structural and thermal properties of *C. angulata* shell were effectively studied through Fourier transform infrared (FTIR), X-ray diffraction (XRD) analysis and thermogravimetric-differential thermal analysis (TG-DTA), respectively. The hydroxyapatite was synthesized from *C. angulata* waste shell by a precipitation method. The synthesized product was characterized through FTIR, XRD, FE-SEM, EDX mapping, HR-TEM and SAED patterns. The antibacterial activity and cell viability assay of prepared hydroxyapatite were also evaluated.

EXPERIMENTAL

The *Crassostrea angulata* shells were collected from Vellar Estuary at Parangipet (Latitude: 11°20′25.55″ N, longitude: 79°45′38.62″ E), India. The important reason of the sampling site chosen was documented as reported [25]. The shells were cleaned with lukewarm tap water for 30 min to eliminate meat and algae, followed by rinsing with flowing distilled water. Subsequently, they were transferred to the oven and heated at 100 °C for 3 h for drying. The dried shells were ground into a fine powder using agate mortar. The powder $CaCO_3$ was again calcined at 900 °C for 3 h to obtain CaO as per the following chemical reaction:

$$CaCO_3 \xrightarrow[\Delta]{900\ °C/3\ h} CaO + CO_2$$
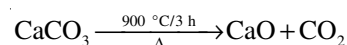
Preparation of hydroxyapatite: The hydroxyapatite nanoparticles were prepared by precipitation method. The calcined CaO from the *C. angulata* sea shells weighed 2.36 g (0.1 mol) and dissolved in 25% pure HNO_3. The solution was dissolved in 75% deionized water to achieve a concentration of 0.1 M $Ca(NO_3)_2$. Subsequently, 0.769 g of prepared 0.06 M $(NH_4)_2HPO_4$ solution was added to the aforesaid solution to obtain Ca/P ratio of 1.67 [25] followed by the addition of 1 M NaOH solution was dropwise under a continuous stirring using a magnetic stirrer to achieve pH 9 value to obtain a milky white precipitate. The precipitation was washed several times using deionized water with Whatman 40 filter paper to remove residuals such as Na and NH_4 [20]. Finally, the white precipitate was dried in a hot air oven at 120 °C. The reaction sequence involved during the preparation of hydroxyapatite is shown below:

$$CaO + 2HNO_3 \longrightarrow Ca(NO_3)_2 + H_2O$$

$$10Ca(NO_3)_2 + 6(NH_4)_2HPO_4 \longrightarrow$$
$$Ca_{10}(PO_4)_6(OH_2) + 6NH_4NO_3$$

$$Ca_{10}(PO_4)_6(OH_2) + 6NH_4NO_3 \xrightarrow{900\ °C/3\ h}$$
$$Ca_{10}(PO_4)_6(OH_2)\ (Hydroxyapatite)$$

RESULTS AND DISCUSSION

Characterization of *C. angulata* waste shells

FTIR spectral studies: Fig. 1 shows the FTIR spectra of non-calcined (a), calcined *C. angulata* shells at 500 °C (b) and 900 °C (c). FTIR spectrum depicted in Fig. 1a show the presence of transmittance peaks at 3414, 2918, 2521, 1790, 1475, 1082, 861, 712 and 699 cm^{-1}. Amongst, the transmittance peaks emerged at 1475, 1082, 861 and 712 cm^{-1} corresponds to the presence of aragonite phase. These transmittance peaks are assigned to in-plane bending (v_4), carbonate out-of-plane bending vibration (v_2), symmetric carbonate stretching vibration (v_1) and asymmetric carbonate stretching vibration (v_3) of $CaCO_3$, respectively. The weak intense peaks appeared around 2918, 2521, 1790 and 699 cm^{-1} also evidenced the presence of aragonite [22]. According to the literature reports, a peak formed at 3414 cm^{-1} corresponds to the OH stretching of water or
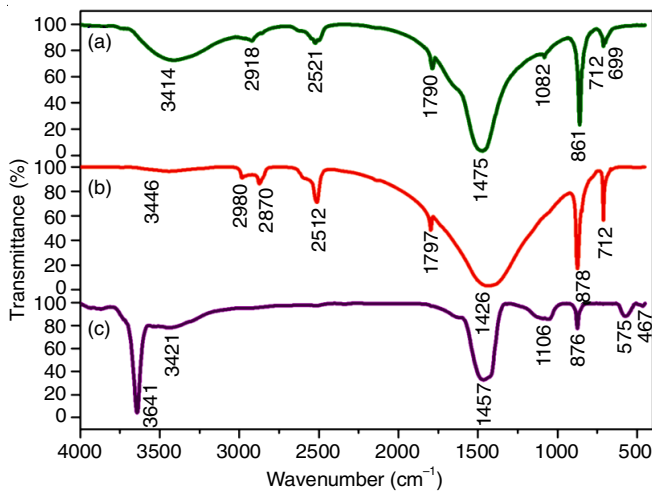
Fig. 1. FTIR spectra of *Crassostrea angulata* shells at room temperature (a), calcined at 500 °C (b) and 900 °C (c)

Fig. 2. XRD pattern of *Crassostrea angulata* shell calcined at 900 °C

Fig. 3. TG-DTA curve of *Crassostrea angulate* shell

hydroxyls [25]. Thus, the non-calcined shells consist of aragonite phase of $CaCO_3$.

Fig. 1b shows the typical FTIR spectrum of *C. angulata* shells calcined at 500 °C. The main characteristic peaks are in-plane bending vibration (v_4) in doublet form at 699 and 712 cm^{-1}, carbonate out-of-plane bending vibration (v_2) at 878 cm^{-1} and v_3 at 1426 cm^{-1}. It was also seen that the symmetric carbonate stretching vibration (v_1) appears at 1082 cm^{-1} is found to be absent. In addition to the characteristic transmittance peaks of calcite, the overlapped peaks corresponding to the calcite phase also formed around 2980, 2870, 2512 and 1797 cm^{-1} [26]. The intensity of OH stretching motions of water or hydroxyls peak is found to be low and shifted to 3446 cm^{-1}. Based on the earlier reports [22,26], it has been confirmed that the above transmittance peaks appeared are mainly due to the formation of calcite phase ($CaCO_3$) upon heating of the *C. angulata* shells at 500 °C.

The shells calcined at 500 °C were further heated at 900 °C and their FTIR spectrum was recorded (Fig. 1c). It was observed that most of the characteristic peaks correspond to calcite phase are disappeared and reduce intensity of carbonate out-of-plane bend-ing vibration (v_2) was found. Also, the intensity of OH$^-$ stretching motions of water or hydroxyls peak deteriorated. Importantly, the well-intense peaks appeared at 1457 cm^{-1} and 3641 cm^{-1} with the evolution of new transmittance peak at 575 cm^{-1}. With the support of literature reports, the new transmi-ttance peaks appeared in Fig. 1c on compared to Fig. 1b indicates that the 900 °C heated sample was decomposed and formed a new chemical phase CaO [25].

Structural analysis of waste shells-XRD: The XRD patterns were recorded for *Crassostrea angulata* shells calcined at 900 °C (Fig. 2) to confirm the CaO formation. It exhibits Bragg's reflection at $2\theta = 29.42°$, 34.63°, 37.43°, 48.27°, 51.26° and 53.98° with (*h k l*) values of (100), (101), (200), (102), (110) and (111), respectively. These diffracted planes were matched with calcium oxide) (JCPDS file No.: 01-077-2010) [27].

Thermal behaviour: Fig. 3 illustrates the TG-DTA curve of *C. angulate* shell, which demonstrates the thermal transfor-
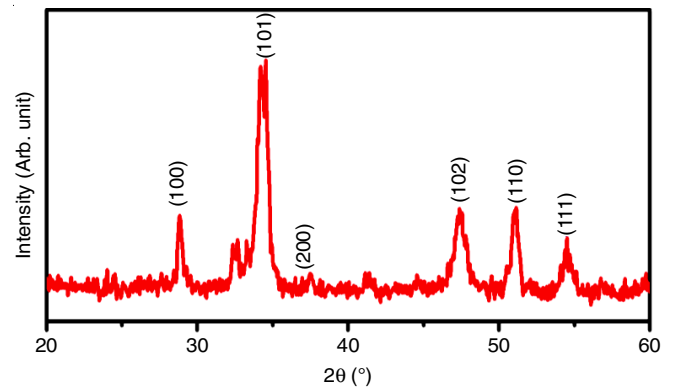
mations of the analyzed sample during the process of controlled heating. The first phase change was observed after 250 °C with small weight loss (~2.37%) and a second phase transformation was appeared in the temperature range of 481-801 °C with weight loss 33.16%. The first phase change was due to dehyd-ration of water from the carbonate in the sample and decompo-sition of organic matter [28]. The second major weight loss occurs due to the thermal dissociation of $CaCO_3$ to CaO [28] with releasing of CO_2. Total weight loss in the sample was 35.53% after the formation of CaO, which formed at 900 °C through calcination.
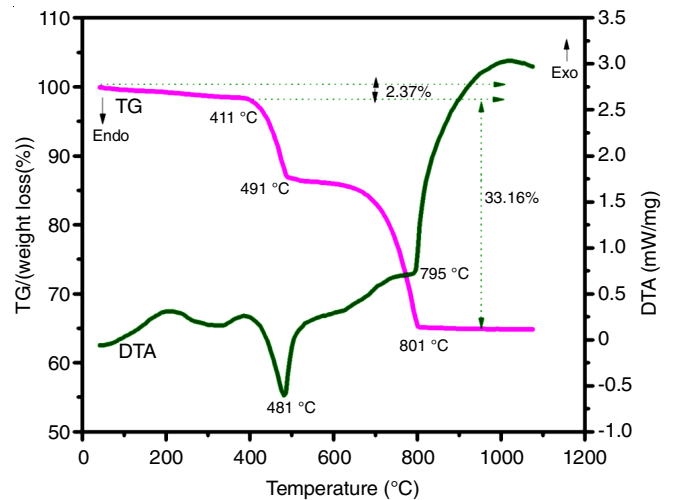
Characterization of hydroxyapatite

XRD studies: The hydroxyapatite was synthesized from *C. angulata* shells and characterized. The XRD pattern (Fig. 4) shows diffraction planes at (111), (002), (210), (211), (112), (300), (202), (301), (310), (311), (113), (222), (213), (321), (123), (410), (402), (004), (322) and (331). The obtained peaks were matched with standard JCPDS data file of hydroxyapatite (09-0432) [20]. As there are no impurity characteristic peaks observed, it is noteworthy to mention that the prepared sample was pure hydroxyapatite.

The average crystallite size of hydroxyapatite was calcu-lated using Scherrer's formula [20]:
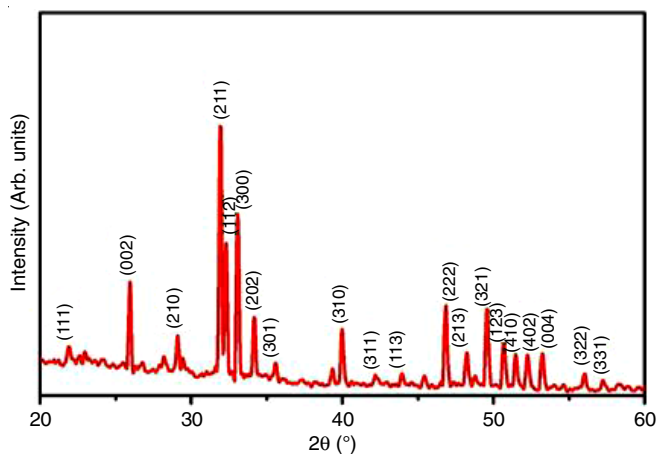
$$D = \frac{k\lambda}{\beta\cos\theta}(nm)$$

Fig. 4. XRD pattern of the hydroxyapatite

Fig. 5. FTIR spectrum of the hydroxyapatite

where D = crystallite size (nm), λ = wavelength (1.5406 Å), k = constant (0.899), β = FWHM and θ = diffracted angle. The calculated average crystallite size of hydroxyapatite was 86.3 nm.

FT-IR spectral studies: The identified transmittance peaks at 3638, 3307, 1655, 1466, 1404, 1030, 963, 868, 705, 636, 602, 566 and 473 cm^{-1} were observed in Fig. 5. The hydroxyapatite can be characterized through the FTIR by the presence of chemical groups such as PO_4^{3-}, OH$^-$ and CO_3^{2-}. According to Youness *et al.* [29], PO_4^{3-} can be characterized by four characteristic peaks namely ν_1 (stretching vibration of the O-P-O bond), ν_2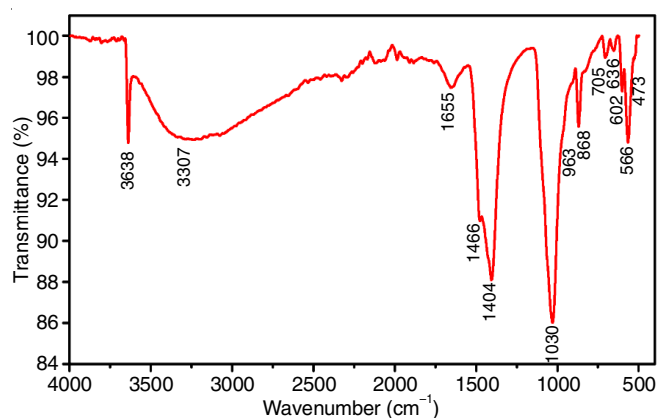 (asymmetric stretching vibration of PO_4), ν_3 (sharp and strong) and ν_4 (triply degenerated bending mode of the O-P-O) at 963, 473, 1030 and 602 and 566 cm^{-1}, respectively. The presences of weak, broad and intense transmittance peaks at 636, 3307 and 3638 cm^{-1} indicate the formation of hydroxyl group (OH$^-$), respectively. The transmittance peaks at 868 (ν_2, out of plane bend) and 1404 and 1466 (ν_3, asymmetric stretching) cm^{-1} observed are accounted for the presence of CO_3^{2-} in hydroxyapatite. Due to the usual formation of meagre amount of $CaCO_3$, a small and low intense absorption peak at 705 cm^{-1} was observed [20].

FE-SEM and EDX mapping studies: The different magnifications of FE-SEM images of hydroxyapatite (Fig. 6a-b) show that the morphology of the prepared hydroxyapatite illustrates
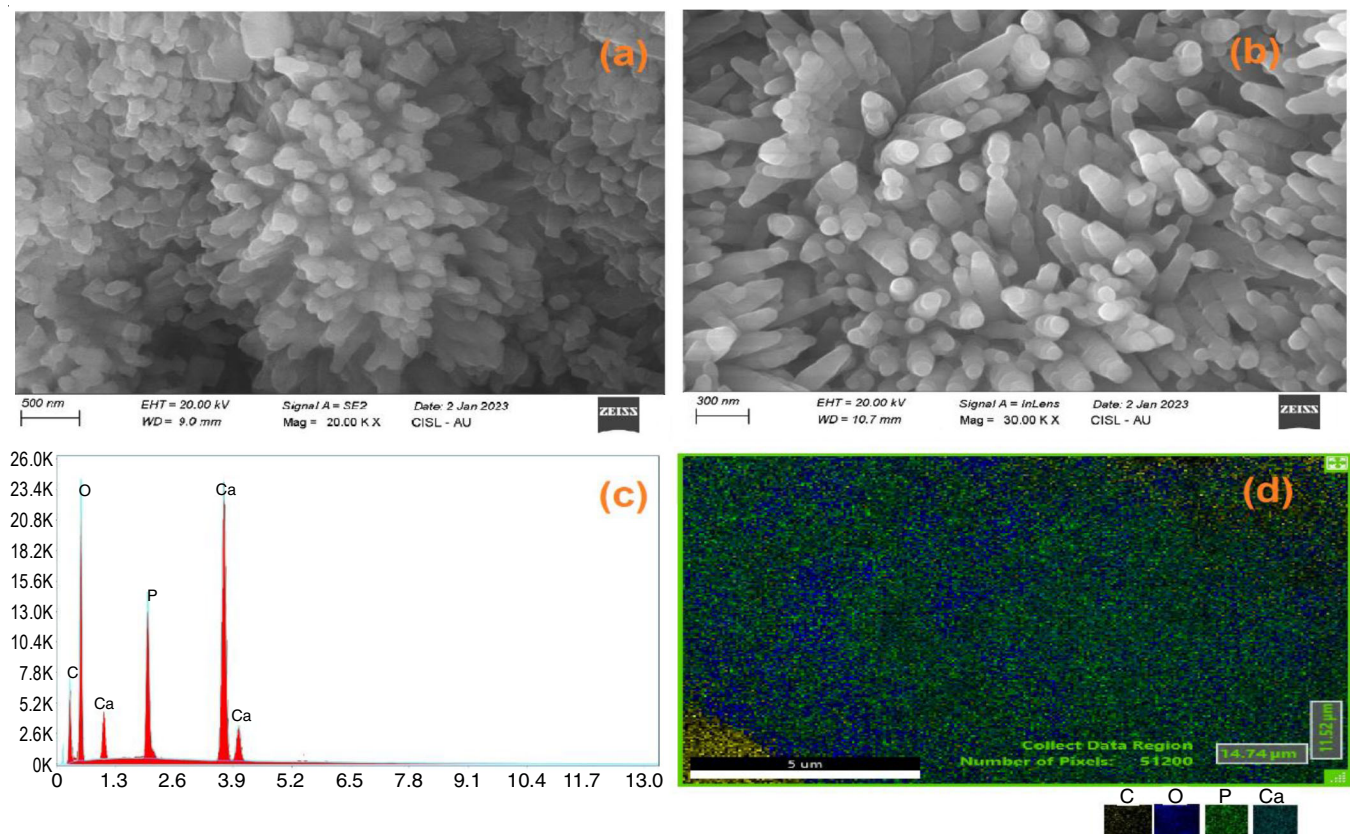

Fig. 6. (a-b) FE-SEM image of hydroxyapatite at two different magnifications, (c) EDX spectrum of hydroxyapatite and (d) EDAX mapping of hydroxyapatite
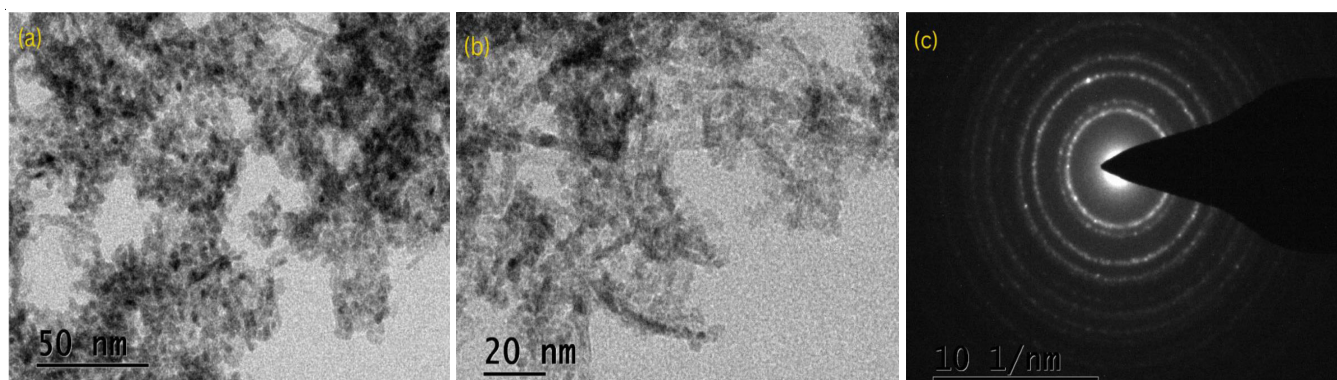
Fig. 7. (a-b) Different magnifications of HRTEM images of hydroxyapatite and the corresponding (c) SAED pattern

clusters of rod-like (majorely) with few hexagonal structures. The formation mechanism of rod-like structure in hydroxyapatite was reported in literature [20,30]. The hydroxyapatite rods were formed through crystallization/nucleation, surface-regulation and growth from the oriented attachment of nanoplates [30]. It can be possible by the higher tendency of nuclei to grow along the *c*-axis. The ions such as phosphate and calcium ions are favourably adsorbed at the *c*-axis. The formation of nanorods could be explained by consequent unidirectional growth of the particles [31]. The observed morphology assists to increase the antibacterial activity, cell viability due to the high surface area and aspect ratio [30]. Fig. 6c-d show the EDX spectrum and mapping of hydroxyapatite. From the EDX spectrum (Fig. 6c), the oxygen, phosphorus, calcium and carbon peaks are visualized, which demonstrates its highest purity.

HR-TEM studies: Fig. 7(a-b) shows the HR-TEM images and the associated selective area electron diffraction (SAED) patterns (Fig. 7c) of hydroxyapatite. The microstructure of hydroxyapatite shows hexagonal rods and irregular needle-like. The HR-TEM results are almost in agreement with FE-SEM results (Fig. 6a-b). The corresponding SAED pattern (Fig. 7c) reveals the presense of crystalline hydroxyapatite, which may be due to the ordered spots presented in the pattern.

Antibacterial activity: The antibacterial activity of hydroxyapatite particles was evaluated against Gram-negative (*E. coli*) and Gram-positive (*S.saprophyticus*) bacterial strains in dark as well as under irradiation of visible light over a 24 h incubation period at 37 ℃. Fig. 8 shows the measured inhibitory zones against *E. coli* and *S. saprophyticus* at 10, 20 and 30 µg/µL. The values were 11, 12 and 17 mm for Gram-negative bacterial strain and 12, 14 and 21 mm for positive bacterial strain, respectively. As expected, in both cases at higher concentration, hydroxyapatite exhibited good antibacterial activity. More interaction between the metal ions and the bacterial wall membranes *via* an electrostatic force or reactive oxygen species (ROS) to damage the cell membrane [7,32] are possible.

Cell viability sudies: The cytocompatibility of hydroxyapatite was assessed through MTT assay test using osteoblast cells (MG-63 cell). Generally, the osteoblast cells are most effectively connected and grown on hydroxyapatite-based biocomposites [18]. Fig. 9 shows the results of hydroxyapatite cytotoxicity testing with normal cell line (a) and various concentrations such as 1000 (b), 250 (c), 125 (d) and 62.5 µg/mL (e).
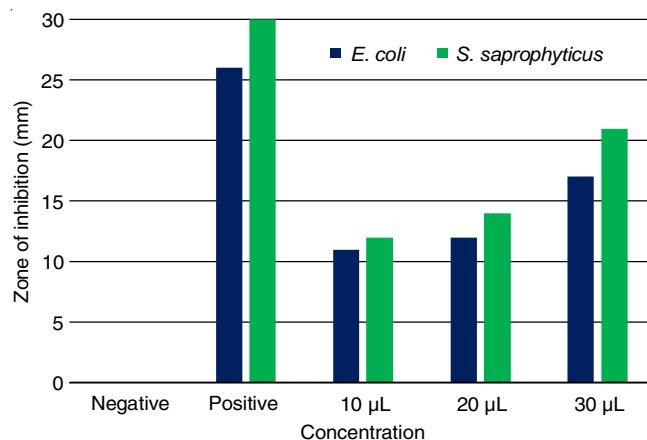

Fig. 8.   Zone of inhibition values of hydroxyapatite against *E. coli* and *S. saprophyticus* in positive, negative control, different concentrations such as 10, 20 and 30 µg/µL

The cells are clearly visible in normal (standard) cell line (Fig. 9a). After treating with hydroxyapatite, some noticeable change is observed in appearance and growth of MG-63 cells (Fig. 9b-e). The cell viability of hydroxyapatite at different concentrations (7.8 -1000 µg/mL) is shown Fig. 10. Cell viability is decreased with increasing hydroxyapatite concentrations. The culture medium interacting with low (7.8 µg/mL) and high (1000 µg/mL) concentrations of extracts exhibit 80% and 15% of cell viability, respectively. The IC_{50} (half-maximal inhibitory concentration) value of hydroxyapatite is 125 µg/mL (Fig. 10) and hydroxyapatite found to be more effective against MG-63 cell. The particle size, moderate crystalline nature, increased solubility and dissolution and high surface area of hydroxyapatite played a major role in its cell viability nature [33].

Conclusion

This work focussed on the preparation of commercial quality hydroxyapatite materials from sea waste shells (*Crassostrea angulata*) through precipitation method for the orthopedic applications. The functional groups, structural characterization and thermal behaviour of *C. angulata* shells confirmed the presence of aragonite, calcite and CaO phase at room temperature, 500 ℃ and 900 ℃, respectively. The XRD patterns shown the formation of hexagonal hydroxyapatite. The average crystallite size of hydroxyapatite was found to be 86.3 nm. The formation of pure hydroxyapatite was also confirmed by the presence of
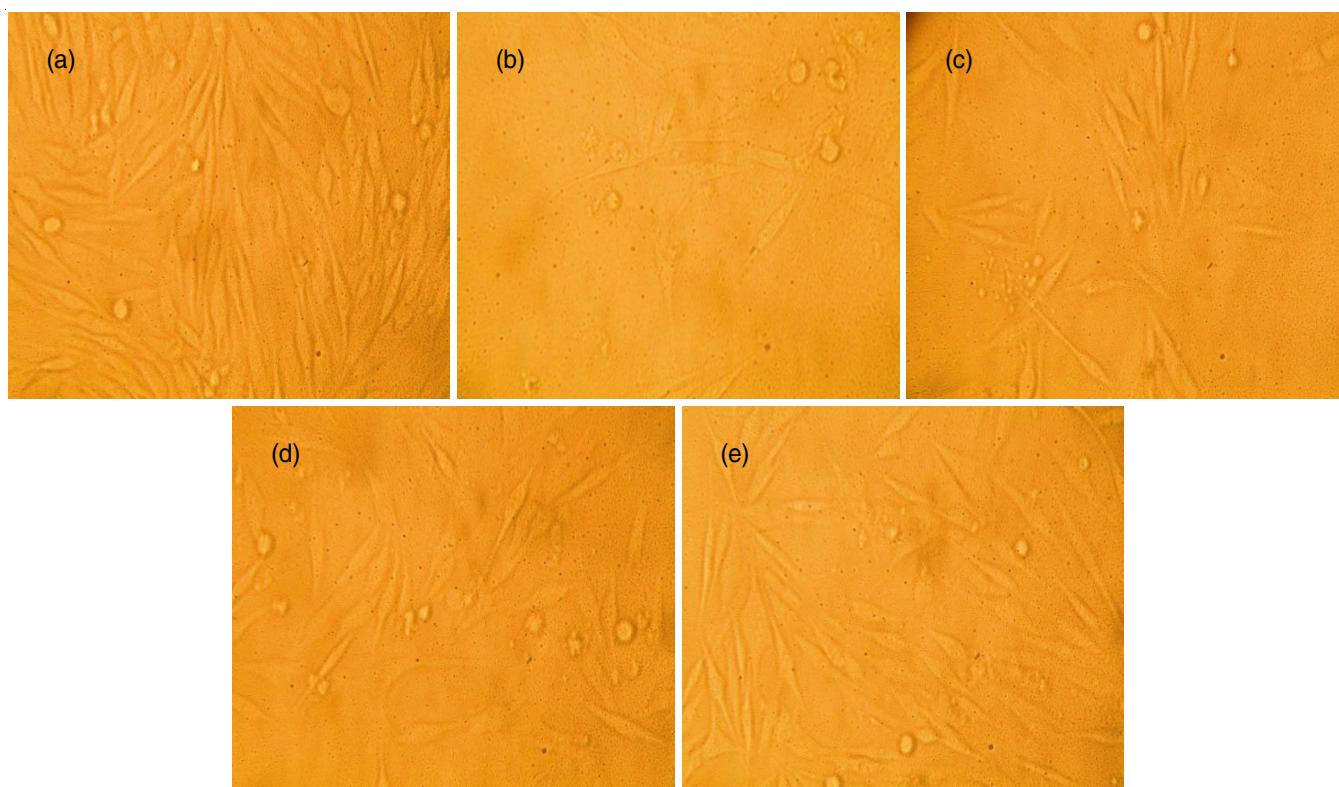
Fig. 9. Cell morphology of MG 63 cells after interacting with liquid extracts of hydroxyapatite. (a) represents the normal cell line, (b-e) show the various concentrations 1000, 250, 125 and 62.5 μg/mL, respectively
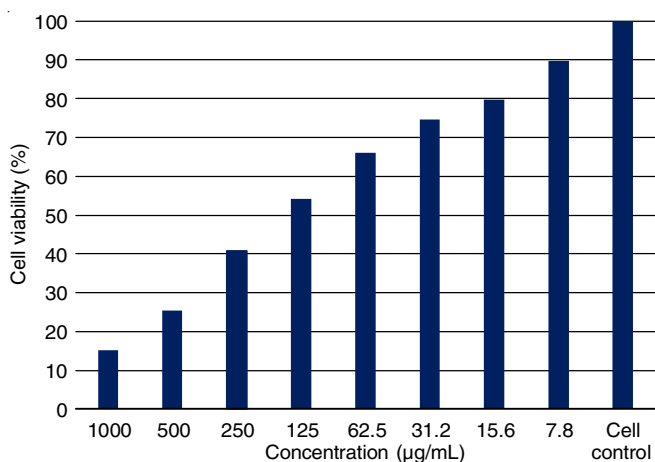

Fig. 10. Cell viability nature of hydroxyapatite at different concentrations

CONFLICT OF INTEREST

The authors declare that there is no conflict of interests regarding the publication of this article.

functional groups such as PO_4^{3-}, OH^- and CO_3^{2-} and elements oxygen, phosphorous, calcium and carbon. Hydroxyapatite displays clusters of rod like (majorly) with few hexagonal structures. The antibacterial capabilities of hydroxyapatite were evaluated against Gram-negative (*E. coli*) and Gram-positive (*S. saprophyticus*) bacterial strains exhibit the good antibacterial activity. The cytocompatibility of hydroxyapatite was assessed through MTT assay using osteoblast cells (MG-63 cell). The cell viability was decreased with increasing hydroxyapatite concentrations and found to be more effective against MG-63 cell. Thus, the prepared hydroxyapatite shows good antibacterial action and cell viability and it can be applied in various biomedical applications.

REFERENCES

1. S. Mondal, S.n Park, J. Choi, T.T.H. Vu, V.H.M.h Doan, T.T. Vo, B. Lee and J. Oh, *Adv. Colloid Interface Sci.*, **321** 103013 (2023); https://doi.org/10.1016/j.cis.2023.103013
2. S.-Y. Peng, Y.-W. Lin, W.-H. Lee, Y.-Y. Lin, M.-J. Hung and K.-L. Lin, *Mater. Chem. Phys.*, **293** 126854 (2023); https://doi.org/10.1016/j.matchemphys.2022.126854
3. R. Verma, S.R. Mishra, V. Gadore and M. Ahmaruzzaman, *Adv. Colloid Interface Sci.*, **315** 102890 (2023); https://doi.org/10.1016/j.cis.2023.102890
4. M.B. Mobaraka, N.S. Pinky, F. Chowdhury, M.S. Hossain, M. Mahmud, M.S. Quddus, S.A. Jahan and S. Ahmed, *J. Saudi Chem. Soc.*, **27** 101690 (2023); https://doi.org/10.1016/j.jscs.2023.101690
5. M. Wang, M. Li, Y. Wang, Y. Shao, Y.n Zhu and S.g Yang, *J. Mater. Chem. B*, **9**, 3401 (2021); https://doi.org/10.1039/D1TB00098E
6. S. Lamkhao, M. Phaya, C. Jansakun, K. Thongkorn, G. Rujijanagul, N. Chandet, P. Bangrak and C. Randorn, *Sci. Rep.*, **9** 4015 (2019); https://doi.org/10.1038/s41598-019-40488-8
7. K. Sinulingga, M. Sirait, N. Siregar and M.E. Doloksaribu, *ACS Omega*, **6**, 34185 (2021); https://doi.org/10.1021/acsomega.1c05921

8.   W. Li, J. Zhou and Y. Xu, *Biomed. Rep.*, **3**, 617 (2015);
     https://doi.org/10.3892%2Fbr.2015.481

9.   S. Lamkhao, M. Phaya, C. Jansakun, N. Chandet, K. Thongkorn, G. Rujijanagul, P. Bangrak and C. Randorn, *Sci. Rep.*, **9**, 4015 (2019);
     https://doi.org/10.1038/s41598-019-40488-8

10. S. Sebastiammal, A.S.L. Fathima, J. Henry, M.A. Wadaan, S. Mahboob, A.M. Wadaan, I.n Manzoor, I. Manzoor, K. Gopinath, M. Rajeswary and M. Govindarajan, *Fermentation*, **8**, 677 (2022);
     https://doi.org/10.3390/fermentation8120677

11. J. Kolmas, E. Groszyk and D. Kwiatkowska-Rohycka, *BioMed Res. Int*., **2014**, 178123, (2014);
     https://doi.org/10.1155/2014/178123

12. K. Pajor, A. Michalicha, A. Belcarz, L. Pajchel, A. Zgadzaj, F. Wojas and J. Kolmas, *Int. J. Mol. Sci*., **23**, 7102 (2022);
     https://doi.org/10.3390/ijms23137102

13. C.B. Ayyanar, K. Marimuthu, B. Gayathri and Sankarrajan, *Polym. Polym. Composit.*, **29**, 1534 (2021);
     https://doi.org/10.1177/0967391120981551

14. M. Sirait, K. Sinulingga, N. Siregar, M.E. Doloksaribu and Amelia, *J. Phys.: Conf. Series*, **2193**, 012039 (2022);
     https://doi.org/10.1088/1742-6596/2193/1/012039

15. G.T. El-Bassyouni, S.S. Eldera, S.H. Kenawy and E.M.A. Hamzawy, *Heliyon*, **6**, e04085 (2020);
     https://doi.org/10.1016/j.heliyon.2020.e04085

16. J. Han, X.-Y. Tong, C.-Y. Rao, J.-M. Ouyang and B.-S. Gui, *ACS Omega*, **8**, 48432 (2023);
     https://doi.org/10.1021/acsomega.3c08180

17. H.Y. Ahmed, N. Safwat, R. Shehata, E.H. Althubaiti, S. Kareem, A. Atef, S.H. Qari, A.H. Aljahani, A.S. Al-Meshal, M. Youssef and R. Sami, *Membranes*, **12**, 408 (2022);
     https://doi.org/10.3390/membranes12040408

18. K. Manivannan, G. Jaganathan and M.A. Sithique, *Asian J. Chem*., **34**, 1073 (2022);
     https://doi.org/10.14233/ajchem.2022.23270

19. M. Cheng, M. Liu, L. Chang, Q.g Liu, C.o Wang, L. Hu, Z. Zhang, W. Ding, L. Chen, S. Guo, Z. Qi, P. Pan and J. Chen, *Sci. Total Environ*., **870**, 161950 (2023);
     https://doi.org/10.1016/j.scitotenv.2023.161950

20. C.S. Kumar, K. Dhanaraj, R.M. Vimalathithan, P. Ilaiyaraja and G. Suresh, *J. Asian Ceramic Soc*., **8**, 416 (2020);
     https://doi.org/10.1080/21870764.2020.1749373

21. G. Borciani, T. Fischetti, G.a Ciapetti, M. Montesissa, N. Baldini and G. Graziani, *Ceram. Int*., **49**, 1572 (2023);
     https://doi.org/10.1016/j.ceramint.2022.10.341

22. N. Suwannasingha, A.t Kantavong, S. Tunkijjanukij, C. Aenglong, H.-B. Liu and W. Klaypradit, *J. Saudi Chem. Soc*., **26**, 101441 (2022);
     https://doi.org/10.1016/j.jscs.2022.101441

23. M. Rehman, M.B. Taj and S.A.C. Carabineiro, *Chemosphere*, **338**, 139477 (2023);
     https://doi.org/10.1016/j.chemosphere.2023.139477

24. C.-F. Chen, Y.-R. Ju, Y.C. Lim, M.-H. Wang, C.-W. Chen and C.-D. Dong, *Marine Pollut. Bull.*, **194** 115228 (2023);
     https://doi.org/10.1016/j.marpolbul.2023.115228

25. K. Dhanaraj and G. Suresh, *Vacuum*, **152**, 222 (2018);
     https://doi.org/10.1016/j.vacuum.2018.03.021

26. Z. Zhou, Y. Wang, S. Sun, Y.g Wang and L. Xu, *Heliyon*, **8**, e11938 (2022);
     https://doi.org/10.1016/j.heliyon.2022.e11938

27. Y.C. Wong and R.X. Ang, *Open Chem.*, **16**, 1166 (2018);
     https://doi.org/10.1515/chem-2018-0127

28. K. Dhanaraj, C.S. Kumar and G. Suresh, *J. Appl. Sci. Comput.*, **5**, 658 (2018).

29. R.A. Youness, M.A. Taha, H Elhaes and M. Ibrahim, *Mater. Chem. Phys.*, **190**, 209 (2017);
     https://doi.org/10.1016/j.matchemphys.2017.01.004

30. I.R. Mary, S. Sonia, D. Mangalaraj, C. Viswanathan, N. Ponpandian and S. Viji, *Appl. Surf. Sci.*, **361**, 25 (2016);
     https://doi.org/10.1016/j.apsusc.2015.11.123

31. M. Sadat-Shojai, M. Atai and A. Nodehi, *J. Braz. Chem. Soc*., **22**, 571 (2011);
     https://doi.org/10.1590/S0103-50532011000300023

32. R.K. Saini, L.P. Bagri and A.K. Bajpai, *Colloids Surf. B Biointerfaces,* **177**, 211 (2019);
     https://doi.org/10.1016/j.colsurfb.2019.01.064

33. M. Manoj, R. Subbiah, D. Mangalaraj, N. Ponpandian, C. Viswanathan and K. Park, *Nanobiomedicine*, **2**, 1 (2015);
     https://doi.org/10.5772/60116